

OPEN

# Thermal stability of tungsten based metamaterial emitter under medium vacuum and inert gas conditions

Manohar Chirumamilla<sup>1\*</sup>, Gnanavel Vaidhyanathan Krishnamurthy<sup>2</sup>, Surya Snata Rout<sup>3</sup>, Martin Ritter<sup>3</sup>, Michael Störmer<sup>2</sup>, Alexander Yu Petrov<sup>1,4</sup> & Manfred Eich<sup>1,2</sup>

Commercial deployment of thermophotovoltaics (TPV) is lacking behind the implementation of solar PV technology due to limited thermal stability of the selective emitter structures. Most of the TPV emitters demonstrated so far are designed to operate under high vacuum conditions ( $\sim 10^{-6}$  mbar vacuum pressure), whereas under medium vacuum conditions ( $\sim 10^{-2}$  mbar vacuum pressure), which are feasible in technical implementations of TPV, these emitters suffer from oxidation due to significant  $O_2$  partial pressure. In this work, the thermal stability of 1D refractory W-HfO<sub>2</sub> based multilayered metamaterial emitter structure is investigated under different vacuum conditions. The impact of the  $O_2$  partial pressure on thermal stability of the emitters is experimentally quantified. We show that, under medium vacuum conditions, i.e.  $\sim 10^{-2}$  mbar vacuum pressure, the emitter shows unprecedented thermal stability up to 1300 °C when the residual  $O_2$  in the annealing chamber is minimized by encapsulating the annealing chamber with Ar atmosphere. This study presents a significant step in the experimental implementation of high temperature stable emitters under medium vacuum conditions, and their potential in construction of economically viable TPV systems. The high TPV efficiency,  $\sim 50\%$  spectral efficiency for GaSb PV cell at 1300 °C, and high temperature stability make this platform well suited for technical application in next-generation TPV systems.

Thermal stability of the selective emitters is one of the key issues in thermophotovoltaics (TPV)<sup>1–8</sup>. TPV provides a viable solution for efficient heat to power conversion, offering theoretical conversion efficiencies up to 85%<sup>2,9–16</sup>. In TPV, a wide variety of thermal sources, such as solar heat and, waste heat from industries and, chemical and nuclear processes, can be turned into electricity using spectrally selective emitters<sup>17–21</sup>. Even though TPV technology has been developed many years ago, the commercial deployment of TPV is hindered due to lack of thermally stable emitter structures at temperatures higher than 1200 °C<sup>5,22–31</sup>. According to the Stefan-Boltzmann law<sup>16</sup>, the radiative power of any object is proportional to  $T^4$ . Further, an ideal emitter should emit with emissivity  $\varepsilon = 1$  for  $E > E_g$  (in-band photons) and  $\varepsilon = 0$  for  $E < E_g$  (out-of-band photons), where  $E$  and  $E_g$  are the thermal photon energy and bandgap energy of the PV cell. Out-of-band photons will not be converted into electricity whereas these photons will be absorbed by the PV cell housing. This will increase the PV cell temperature and thereby further decrease the TPV efficiency. The out-of-band photons can be recycled using front surface filters or a mirror behind the PV cell. Front surface filters placed between the emitter and PV cell revert back the out-of-band photons to the emitter<sup>32–34</sup>. Alternatively, by introducing a highly reflective mirror surface at the rear of the PV cell, out-of-band photons can be directed back to reheat the emitter<sup>29,35</sup>. Still, the filters and mirrors have residual absorptivity which might result in a reduction of efficiency. Thus, spectrally selective TPV emitters operating at high temperatures might be required even in combination with filters and mirrors to obtain high conversion efficiency.

<sup>1</sup>Institute of Optical and Electronic Materials, Hamburg University of Technology, Eissendorfer Strasse 38, Hamburg, 21073, Germany. <sup>2</sup>Institute of Materials Research, Helmholtz-Zentrum Geesthacht Centre for Materials and Coastal Research, Max-Planck-Strasse 1, Geesthacht, 21502, Germany. <sup>3</sup>Electron Microscopy Unit, Hamburg University of Technology, Eissendorfer Strasse 42, Hamburg, 21073, Germany. <sup>4</sup>ITMO University, 49 Kronverkskii Avenue, Saint Petersburg, 197101, Russia. \*email: [manohar.chirumamilla@tuhh.de](mailto:manohar.chirumamilla@tuhh.de)

The highest temperature stability of structured thermal emitters of 1400 °C was achieved so far at high vacuum conditions<sup>1,2</sup>, of  $10^{-5}$ – $10^{-6}$  mbar vacuum pressure, with an application of turbomolecular pumps. However, these working conditions are economically not viable in the commercialization of TPV technology. At medium vacuum condition of  $10^{-2}$  mbar, which can be achieved without turbomolecular pump, the thermal stability of metal-based emitters drastically decreases at high temperatures<sup>1,7,26,36</sup>. For example, we have shown that 1D multilayered metamaterial emitters from W-HfO<sub>2</sub> nanolayers can be thermally stable only up to 1000 °C under  $10^{-2}$  mbar medium vacuum pressure<sup>1,36</sup>. The oxidation of refractory metals is limited only by diffusion of oxygen through the protection layers, such as HfO<sub>2</sub><sup>4,37,38</sup>. The amount of transported oxygen is dependent on the residual O<sub>2</sub> partial pressure and temperature. From our study on the stability of W-HfO<sub>2</sub> multilayered metamaterial at different vacuum pressures<sup>1</sup>, we learned that for the same annealing time a 10-fold reduction in the residual O<sub>2</sub> partial pressure can help to improve the thermal stability of the metamaterial structure by approximately 150 °C higher. Thermal stability of the emitters can be further improved by minimizing the residual O<sub>2</sub> in the annealing chamber. In order to deploy TPV technology over a large scale, TPV systems should be operated under a reasonable cost and thermal emitters should sustain at high temperatures. TPV systems operating under medium vacuum and enclosed with inert gas conditions can boost the deployment of efficient TPV systems. Inert gases, such as Ar, can be used to minimize the O<sub>2</sub> partial pressure in the medium vacuum.

In the current work, W and HfO<sub>2</sub> materials have been used to construct 1D metamaterial emitter. W has been chosen due to its high melting point of 3422 °C, low-emissivity in the infrared region and low-vapour pressure compared to other refractory metals. Refractory oxides, nitrides, carbides and borides can be used as dielectric material to construct the metamaterial. However, borides, carbides and nitrides often have metal-like optical properties and exhibit in-band and out-of-band emission<sup>2,34</sup>. Refractory oxides, such as Al<sub>2</sub>O<sub>3</sub>, HfO<sub>2</sub>, and ZrO<sub>2</sub> show dielectric properties and are stable in oxidizing atmospheres. Thermal stability of the Al<sub>2</sub>O<sub>3</sub> based emitters demonstrated so far lies below 1300 °C<sup>28,39–41</sup>. ZrO<sub>2</sub> suffers from phase change transition (from monoclinic to tetragonal at around 1000 °C) at high temperatures<sup>42,43</sup>. Whereas HfO<sub>2</sub> also undergoes a similar monoclinic to tetragonal phase transition but around 1700 °C<sup>44</sup>, providing better phase stability at a higher temperature. Thus, HfO<sub>2</sub> was chosen in the present work.

The thermal stability experiments were performed in a vacuum chamber that is enclosed in an Ar gas atmosphere. Multilayered 1D W-HfO<sub>2</sub> based metamaterial structure is investigated for high temperature stability under  $2 \times 10^{-2}$  mbar vacuum conditions enclosed with argon gas atmosphere with 20 ppm residual oxygen. 1D metamaterial emitter shows exceptional thermal stability up to 1300 °C and to the best of our knowledge 1300 °C is the highest temperature reported for an emitter so far operating under medium vacuum condition. Presented 1D emitter exhibits a spectral TPV efficiency of 50% for GaSb PV cell with a bandgap of 0.72 eV.

## Results and Discussion

Figure 1a shows the schematic of the investigated W-HfO<sub>2</sub> emitter structure, six bilayers of W and HfO<sub>2</sub>, with a thickness of 30 and 100 nm each, respectively, are sandwiched between a top protective HfO<sub>2</sub> layer and bottom thick W layer with a thickness of 100 nm and 200 nm, respectively. Due to the total thickness of the metal layers in the metamaterial emitter structure, light transmission through the emitter structure can be neglected. According to Kirchhoff's law of thermal radiation<sup>45,46</sup> the emissivity of a hot radiating body equals its absorptivity. Thus, the emissivity can be directly deduced from its absorptivity. The spectral selectivity of the emitter should be maintained at different emission angles. Otherwise, an efficiency reduction can be expected due to out-of-band photons emitted at oblique angles. As we have shown previously, a 1D W-HfO<sub>2</sub> metamaterial emitter shows constant spectral selectivity up to 70° incidence angles<sup>36</sup>, which is one of the main advantages of metamaterial emitters in comparison to resonance-based emitters<sup>11</sup>.

Figure 1b shows the cross-sectional scanning electron microscope (SEM) image of the as-fabricated emitter structure, where the distinction between HfO<sub>2</sub> and W layers can be clearly seen with a smooth interfacial surface. The measured absorptivity/emissivity spectrum of the as-fabricated emitter structure is shown in Fig. 1c-black trace. The metamaterial is designed to operate at high temperatures up to 1400 °C. In accordance with the black-body radiation at 1400 °C, the band-edge spectral characteristics were tailored to obtain high and low emissivities below and above, respectively, the spectral-cutoff around 1.72 μm of GaSb PV cell. Based on the previous works<sup>1,36</sup>, we have optimized the metal and dielectric layer thickness values in order to minimize the residual absorption in the mid-infrared region. A 30 nm thin film based metamaterial (Fig. 1c) shows around 2× less mid-infrared absorptivity/emissivity compared to a 20 nm thin film metamaterial emitter<sup>1,36</sup>. Thermal photons coming from a radiative blackbody span over a wide range of wavelengths, where most of the energy is residing in the long-wavelength regime. Thus, reducing the emissivity in the long-wavelength region will avoid heating of the PV cell housing package and thus help to maintain the external quantum efficiency of the PV cell<sup>47</sup> without the use of additional front surface filters, which would impose another restriction on the thermal stability<sup>32–34</sup>. The reduced absorptivity/emissivity in mid-infrared range with larger W thickness can be attributed to the change in electron collision frequency of the metal films, where it decreases with an increment in film thickness. This contributes to the reduction in the imaginary part of the dielectric function  $\epsilon''$  in the mid-infrared range, thus improving the reflectivity of the metal<sup>48,49</sup>. The absorptivity/emissivity spectrum clearly shows a step function-like band-edge spectral characteristics around 1.72 μm, where high/low absorptivities/emissivities, respectively, are absorbed below and above the wavelength corresponding to the cut-off wavelength at 1.72 μm of the PV cell. In the mid-infrared region, the absorptivity/emissivity is around 7%, which is close to the absorptivity/emissivity of the bulk W metal.

Figure 2 shows the XRD analysis of the metamaterial structure before and after annealing at 1400 °C for 6 h under vacuum pressure of  $2 \times 10^{-6}$  mbar, where both, as-prepared and heat-treated, structures exhibit polycrystalline nature. W has the bcc structure (JCPDS 00-004-0806) of  $\alpha$ -phase with (110), (200) and (211) planes at  $2\theta = 40.3^\circ$ ,  $58.3^\circ$  and  $73.2^\circ$ , respectively, and HfO<sub>2</sub> has a monoclinic structure (JCPDS 034-0104), with (-111),

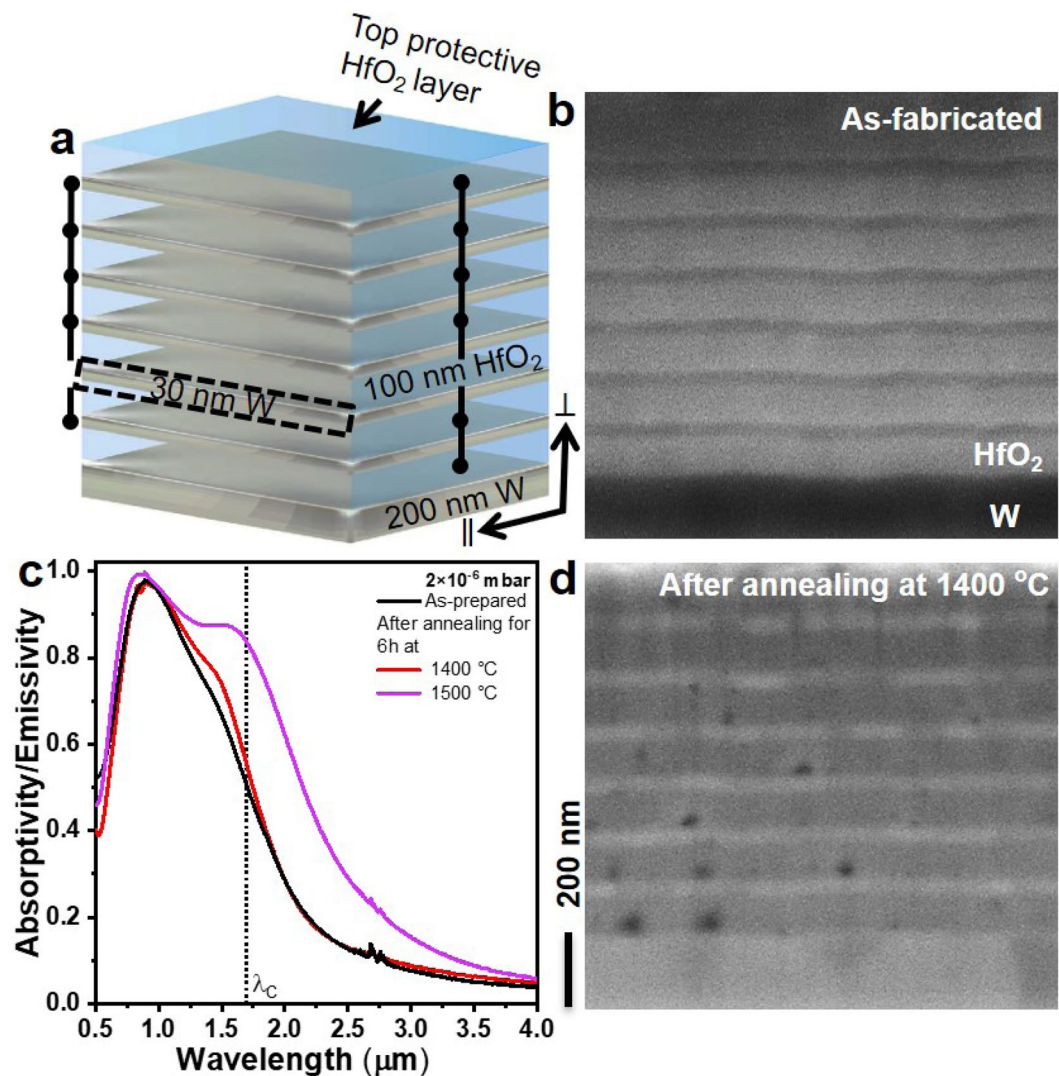


**Figure 1.** (a) Schematic illustration of the W-HfO<sub>2</sub> emitter structure. (b,d) Cross-sectional SEM images of the emitter structure for as-fabricated, and after annealing at 1400 °C for 6 h under vacuum pressure of  $2 \times 10^{-6}$  mbar, respectively. (c) The measured absorptivity/emissivity spectra of the emitters shown in (b,d) are taken at room temperature.  $\lambda_c$  represents the cut-off wavelength at 1.72 μm, corresponding to the bandgap of the GaSb PV cell at 0.72 eV.

(-212) and (-312) planes at  $2\theta = 28.3^\circ$ ,  $49.1^\circ$  and  $62.4^\circ$ , respectively. After annealing at 1400 °C for 6 h, the diffraction peaks of W and HfO<sub>2</sub> were narrowed, which confirms the increment in W and HfO<sub>2</sub> grain sizes. W and HfO<sub>2</sub> grain sizes were calculated using the Scherrer formula<sup>50,51</sup> taking into account the (110) and (-111) reflexes, respectively. For the as-prepared structure, W and HfO<sub>2</sub> show grain sizes of 13 and 12 nm, whereas after annealing at 1400 °C grain sizes were increased to 21 and 27 nm, respectively.

Figure 3 shows the annealing schemes used in the present work. In Fig. 3a, the thermal stability of the metamaterial emitter is investigated using a high vacuum chamber oven operating at  $2 \times 10^{-6}$  mbar vacuum pressure surrounded by ambient air atmosphere, whereas in Fig. 3b the emitter is annealed in a medium vacuum chamber oven operating at  $2 \times 10^{-2}$  mbar vacuum pressure surrounded by ambient air atmosphere. In the schematic shown in Fig. 3c, a medium vacuum chamber oven operating at  $2 \times 10^{-2}$  mbar vacuum pressure encapsulated by Ar atmosphere is used for annealing experiments. As a first step, we have annealed the metamaterial structures in a high vacuum chamber as shown in Fig. 3a. The emitter structure is subjected to the annealing temperature of 1500 °C for 6 h under  $2 \times 10^{-6}$  mbar vacuum pressure. The measured absorptivity/emissivity spectra taken at room temperature after annealing at 1400 °C is shown in Fig. 1c-red trace, which is almost identical to the spectral features observed in the as-fabricated emitter structure. The corresponding cross-sectional SEM image of the emitter structure is shown in Fig. 1d. The W layers show rough surfaces due to grain growth at high temperatures, and voids in the HfO<sub>2</sub> layers owing to grain growth (Fig. 2) through intra-layer diffusion of HfO<sub>2</sub>. Except for these minor structural changes, the metamaterial emitter structure shows exceptional spectral stability and structural integrity after annealing at 1400 °C for 6 h under  $2 \times 10^{-6}$  mbar vacuum pressure. The O<sub>2</sub> partial pressure in the vacuum chamber is estimated to be in the order of  $4 \times 10^{-7}$  mbar (assumed to be 21% of vacuum pressure

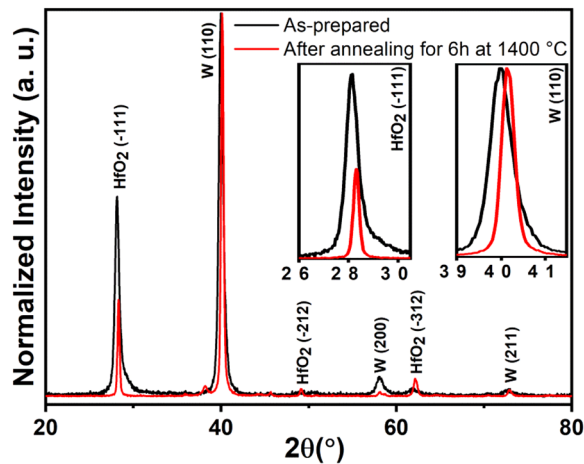


**Figure 2.** XRD spectra of the emitter before and after annealing at 1400 °C for 6 h under vacuum pressure of  $2 \times 10^{-6}$  mbar. XRD spectra were normalized with respect to dominant (110) peak of bcc W. Insets show the magnified view of HfO<sub>2</sub> and W reflexes for (−111) and (110) planes, respectively.

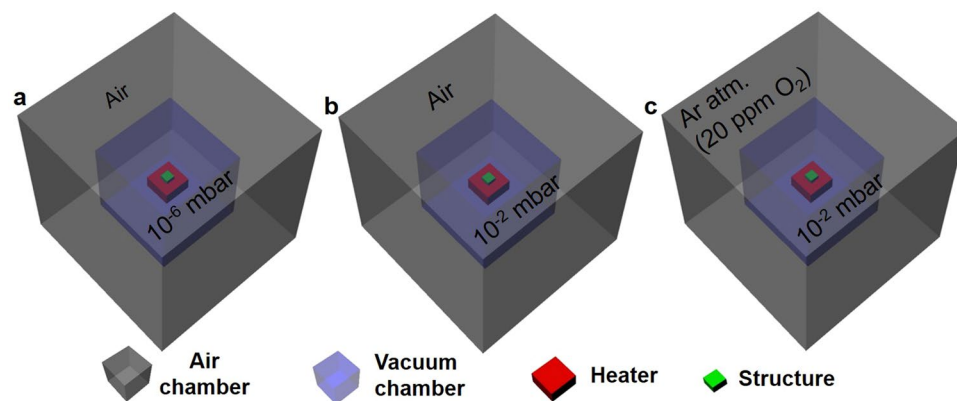


**Figure 3.** Schematic presentation the annealing schemes used to investigate the thermal stability of the emitter structure. Objects are not in scale.

coming as leakage into vacuum from air environment)<sup>52</sup>. No traces of W oxidation is seen, any formed volatile tungsten oxides sublime immediately and leave voids in the W layers at these temperatures<sup>1</sup>. At 1500 °C, the metamaterial emitter structure shows spectral degradation, i.e., high emissivity in the long-wavelength region due to the structural changes in the emitter structure, owing to grain growth and void formation in HfO<sub>2</sub> layer. Under high vacuum conditions, the thermal stability of the 1D metamaterial emitter is limited by the intrinsic structural changes in W and HfO<sub>2</sub> layer.

In order to study the influence of medium vacuum condition on the spectral/structural stability of the 1D metamaterial structure, the emitter structures are annealed under  $2 \times 10^{-2}$  mbar vacuum pressure, showed in Fig. 3b. The measured absorptivity/emissivity spectra of the metamaterial emitter taken at room temperature for as-fabricated and, after annealing at 1000 and 1100 °C for 6 h under  $2 \times 10^{-2}$  mbar vacuum pressure is shown in Fig. 4a. No change in the optical spectrum of the emitter is observed after annealing at 1000 °C (Fig. 4a-orange trace), whereas spectral degradation, an increase of absorptivity/emissivity throughout the spectral region, is clearly observed after annealing at 1100 °C (Fig. 4a-blue trace). The residual O<sub>2</sub> partial pressure in the vacuum chamber is in the order of  $4 \times 10^{-3}$  mbar. The top protective HfO<sub>2</sub> layer limits oxygen diffusion for 6 h at 1000 °C. W and HfO<sub>2</sub> films show nanocrystalline nature (Fig. 2) and (usually nanocrystalline materials contain grain boundaries) offer various diffusion channels. Since a diffusion process is dependent on temperature, we observe that for the same time at 1100 °C progression of oxygen diffusion from the external environment through HfO<sub>2</sub> layer to the W layers is oxidizing the W surfaces<sup>1,36</sup>. The cross-sectional SEM image of the metamaterial emitter structure after annealing at 1100 °C is shown in Fig. 4b, where voids are clearly seen in W and HfO<sub>2</sub> layers. Oxygen can diffuse in atomic form through HfO<sub>2</sub> by interstitial or exchange process<sup>53,54</sup>. This might alter the HfO<sub>2</sub> crystal structure, promote grain growth and lead to the formation of voids in the HfO<sub>2</sub> layer. Oxygen diffusion through HfO<sub>2</sub> and transportation via voids oxidizes the W and creates holes in W layer due to sublimation of volatile W oxides<sup>55,56</sup>. The grain growth of HfO<sub>2</sub> can also rupture the W layers<sup>1</sup>.



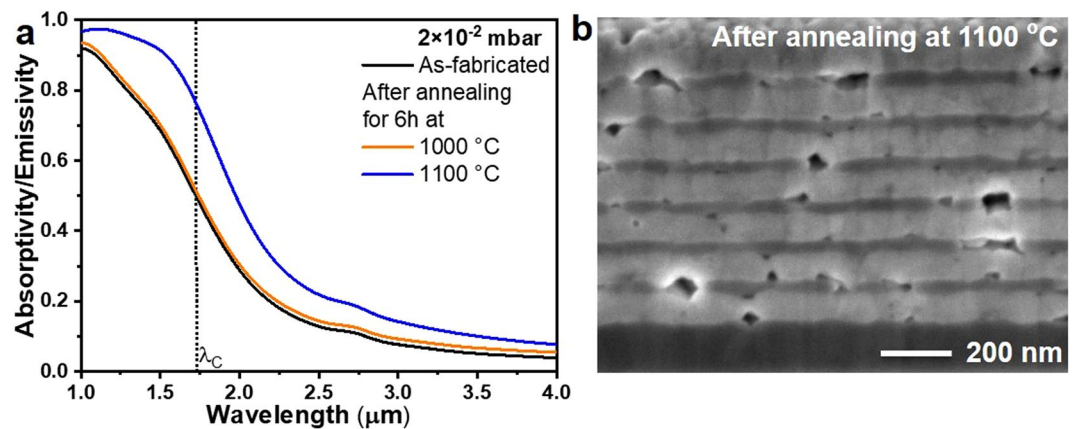


**Figure 4.** (a) Absorptivity/emissivity spectra of the emitter, taken at room temperature, for as-fabricated, and after annealing at 1000 °C and 1100 °C for 6 h under medium vacuum pressure of  $2 \times 10^{-2}$  mbar. (b) Cross-sectional SEM image of the emitter structure after annealing at 1100 °C for 6 h under  $2 \times 10^{-2}$  mbar vacuum pressure.

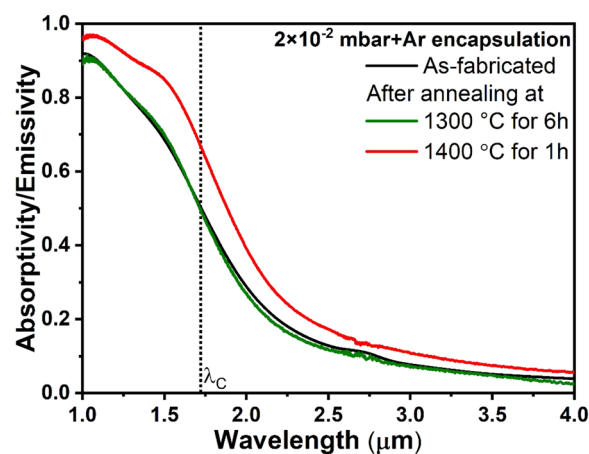


**Figure 5.** Experimental spectral absorptivity/emissivity of the emitter structure measured at room temperature for as-fabricated and after annealing at 1300 °C for 6 h and 1400 °C for 1 h under  $2 \times 10^{-2}$  mbar vacuum pressure and encapsulating the vacuum chamber with Ar atmosphere.

Thus, metamaterial emitter structures show a thermal stability limit of 1000 °C under medium vacuum condition of  $2 \times 10^{-2}$  mbar vacuum pressure, which can be improved further by reducing the residual  $O_2$  content in the annealing chamber.

In order to minimize the residual  $O_2$  content in the medium vacuum condition, we have encapsulated the annealing chamber with Ar atmosphere, Fig. 3c. The purged argon has the purity of 99.999%, due to residual air in the encapsulation region we have measured the  $O_2$  content in the encapsulated area of 20 ppm (see experimental section). Thus, the effective  $O_2$  partial pressure in the annealing chamber is dramatically reduced from  $\sim 10^{-3}$  to  $10^{-7}$  mbar. Thermal stability of the 1D metamaterial emitter structure is investigated by annealing the emitter structures up to 1400 °C, and the corresponding typical optical spectra after annealing at 1300 and 1400 °C are shown in Fig. 5. After annealing at 1300 °C for 6 h, the optical spectrum shows no variance compared to the as-fabricated structure and the corresponding cross-sectional SEM image of the emitter is shown in Fig. 6a. No visible damage to the W layers is observed, such as voids due to sublimation of W oxides. However,  $HfO_2$  layers still show voids, particularly in the top layers, but the number of voids observed in the structure is much less than in the case observed for medium vacuum conditions without Ar gas encapsulation (Figs. 3b and 4b). The reason is the decrease of  $O_2$  partial pressure in the annealing chamber due to Ar gas encapsulation, and thereby reduction of the oxygen transfer through  $HfO_2$  and subsequent structural changes. When the metamaterial emitter is annealed at 1400 °C for 1 h, the optical spectrum shows higher absorptivity/emissivity below and above the  $\lambda_c$  (Fig. 5-red trace), i.e. spectral degradation. A typical cross-sectional SEM image of the metamaterial structure after annealing at 1400 °C is shown in Fig. 6b, which clearly shows the voids in  $HfO_2$  as well as W layers (white-dotted rectangles). We have taken multiple cross-sectional images and found that the visible combined cross-sectional area of voids formed in the top thin W layers is higher than in the lower thin W layers, whereas the bottom W layers are left largely intact (Fig. 6b). Since, oxygen is diffusing from the external environment to the

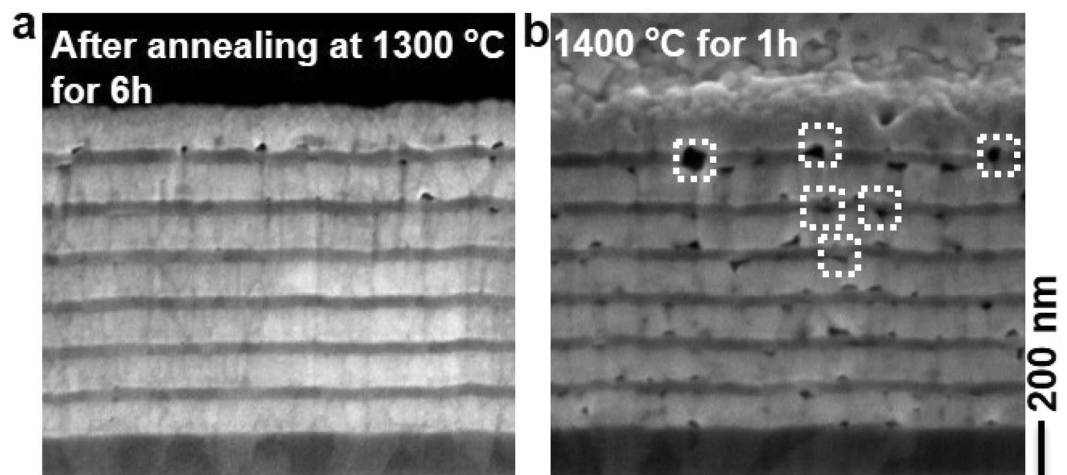


**Figure 6.** Cross-sectional SEM image of the emitter structures after annealing at 1300 °C for 6 h (a) and 1400 °C for 1 h (b) under  $2 \times 10^{-2}$  mbar vacuum pressure and encapsulated by the Ar atmosphere. Note that a thin Au/C layer is sputter deposited on the sample prior to the FIB milling to prevent charging of the substrate during imaging. White dotted boxes indicate visible cross-sectional areas of voids formed after annealing.

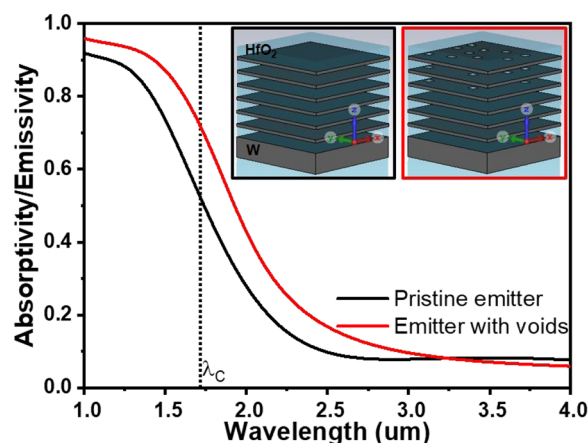


**Figure 7.** Calculated absorptivity/emissivity spectra of the emitter structure for pristine emitter and emitter with voids, the corresponding unit cell schematics are shown in the inset.

emitter, a 100 nm top protective  $\text{HfO}_2$  layer successfully prevents residual oxygen diffusion up to 1300 °C for 6 h, whereas at 1400 °C, according to the temperature enhanced oxygen diffusion, larger voids are formed randomly in the W layers already after 1 h annealing due to subsequent sublimation of volatile W oxides.

Thus, oxygen transport through  $\text{HfO}_2$  is governed by partial oxygen pressure and temperature, which leads to grain growth in  $\text{HfO}_2$  and formation of voids in the layer. This, in turn, leads to a rupture of the W layers next to the  $\text{HfO}_2$  layers and to voids as observed in the sample after annealing at 1100 °C without encapsulation. Some of the tungsten atoms in the upper layers oxidize and leaves the structure due to sublimation of volatile W oxides. The results of annealing at 1300 °C and 1400 °C test can be interpreted as an accelerated test. We see that the encapsulated structure degrades at 1300 °C for 6 h to a smaller degree than at 1400 °C for 1 h. In fact, there is at least a 10 times durability improvement per 100 °C. With that, our emitter should operate more than 1000 h at 1100 °C in an encapsulated vacuum chamber. The exact determination of the scaling factor will be the goals of our future investigations. In order to understand the change in the absorptivity/emissivity of the emitter after annealing at 1400 °C, we have calculated absorptivity/emissivity spectra of the emitter structure without any structural changes (pristine emitter, Fig. 7-black trace) shows high and low emissivities below and above the cut-off wavelength, respectively, similar to the as-fabricated structure shown in Fig. 5. When the voids are implemented as holes in the top three 30 nm W layers of the emitter (schematic of the unit cell is shown in the inset of Fig. 7), the calculated absorptivity/emissivity spectrum shows a red shift in spectral profile and higher emissivities below and above the cut-off wavelength position compared to pristine emitter. The red shift of the spectrum is expected and can be explained by the decrease of the total amount of W content in the thin layers. According to the effective

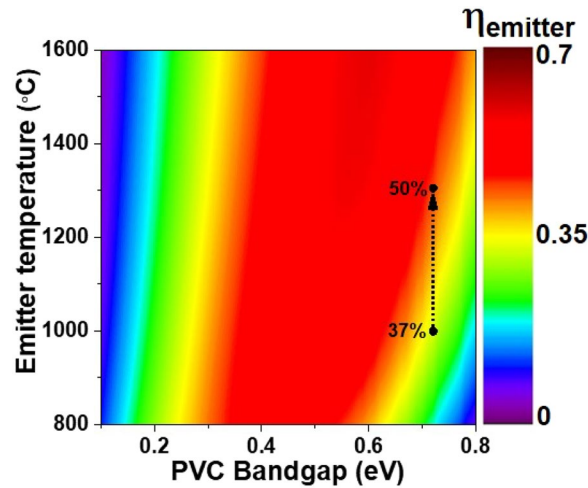


**Figure 8.** The TPV conversion efficiency of 1D metamaterial emitter structure. Contour map shows the emitter efficiency  $\eta_{emitter}$  of 1D layered metamaterial emitter structure for temperature versus PV cell bandgap energy.

medium approximation<sup>36,57</sup> the effective permittivity will change due to vacuum holes shifting the near zero epsilon point to longer wavelengths.

Thus, under medium vacuum condition with reduced residual  $O_2$  content, the thermal stability limit of the 1D metamaterial emitter is increased to 1300 °C. Reducing further the residual oxygen content in the encapsulated area, the thermal stability of the emitters can be matched with the case of high vacuum conditions, up to 1400 °C.

The spectral efficiency of the emitter,  $\eta_{emitter}$ , is calculated using Eq. 1.

$$\eta_{emitter} = \int_{E_g}^{\infty} \frac{E_g}{E} \varepsilon(E) I_{BB}(E, T_{emitter}) dE / \int_0^{\infty} \varepsilon(E) I_{BB}(E, T_{emitter}) dE \quad (1)$$

where  $\varepsilon$ ,  $E$ ,  $T_{emitter}$  and  $I_{BB}$  correspond to the spectral emissivity, photon energy, emitter temperature and black-body spectral power density at the emitter temperature, respectively. Figure 8 shows the  $\eta_{emitter}$  with respect to temperature and PV cell bandgap. When the metamaterial emitter is operating under medium vacuum conditions and the annealing chamber is encapsulated in Ar atmosphere, it shows 37% efficiency at 1000 °C for PV cell bandgap of  $E_g = 0.72$  eV (GaSb PV cell). When the temperature is raised to 1300 °C the emitter shows 50% spectral efficiency. If a blackbody radiator is used instead of the metamaterial emitter, it will show only 16% conversion efficiency at 1300 °C. Thus, 1D multilayered metamaterial emitter exhibits  $3.1 \times$  higher efficiency than a blackbody operating at 1300 °C. It should be mentioned that calculated efficiency is based on spectral absorptivity measured at normal incidence. But due to weak angle dependence of absorptivity/emissivity as discussed earlier, we expect that this efficiency holds also for wide angle emission, up to  $\pm 70^\circ$ <sup>36</sup>.

## Conclusion

In summary, we have investigated the effect of residual  $O_2$  partial pressure on the thermal stability of the emitter structures at high temperatures. Under high vacuum conditions,  $\sim 10^{-6}$  mbar vacuum pressure, the metamaterial emitter shows unprecedented thermal stability up to 1400 °C. At temperatures higher than 1400 °C, the thermal stability of the emitter structure is limited by the structural changes in  $HfO_2$  and the oxidation does not play any role in the emitter degradation. Under medium vacuum conditions,  $\sim 10^{-2}$  mbar vacuum pressure, the emitter structure shows thermal stability up to 1000 °C, and at higher temperatures W and  $HfO_2$  layers in the emitter structure show degradation due to oxidation. By encapsulating the annealing chamber operating under medium vacuum condition with Ar atmosphere, the metamaterial emitter structure shows outstanding spectral/structural stability of 6 hours at a temperature of 1300 °C. The cumulative effect of medium vacuum condition and inert gas encapsulation improves the thermal stability limit of 1D emitters to 1300 °C, which paves the way towards building the next generation TPV systems.

## Methods

**1D metamaterial emitter structure fabrication.** Metamaterial emitters with W and  $HfO_2$  thin films were fabricated on  $5 \times 5$  mm<sup>2</sup> single crystalline sapphire substrates ([1–102] orientation) by radio frequency and direct current magnetron sputtering at a rate of 0.2 and 0.09 nm s<sup>−1</sup>, respectively. All the layers are grown sequentially at argon (99.99999%) gas pressure of  $2 \times 10^{-3}$  mbar. The W and  $HfO_2$  sputtering targets with 99.95% purity were purchased from Sindlhauser Materials. Cross-sectional SEM images of the emitter structures were prepared using a focused-ion beam (FIB, FEI Helios G3 UC) operating at 30 keV. The secondary electron images were taken under low kV (2 kV) and high-resolution immersion mode using a through lens detector (TLD).

**Thermal annealing.** Emitter structures were annealed in a high-temperature heating stage (Linkam, TS1500) at  $2 \times 10^{-2}$  mbar vacuum pressure using a rough vacuum pump, and in a high-temperature vacuum

furnace (RD-G WEBB) at  $2 \times 10^{-6}$  mbar vacuum pressure. The temperature was ramped at a rate of  $10^\circ\text{C min}^{-1}$ .  $\text{O}_2$  concentration in the encapsulated area is measured using an  $\text{O}_2$  sensor (Sensor type: SO-B0-010, in the range up to 2000 ppm, purchased from SENSORE Electronic GmbH) and it is assembled on a generic sensor board. Ar gas (99.999% from Linde) at a pressure of 3 bar is used to encapsulate the annealing chamber.

**Absorptivity/emissivity measurements.** Absorptivity/emissivity spectra of the emitter structures, for as-fabricated and after annealing at high-temperatures, were obtained by measuring reflectivity spectra using a UV-Vis-NIR spectrometer (PerkinElmer Lambda 1050) and a Fourier transform infrared spectrometer (FTIR-Vertex 70, Bruker), in the ranges of 0.3 to  $2.5\ \mu\text{m}$  and 1 to  $5\ \mu\text{m}$ , respectively. Where, absorptivity  $\alpha = 1 - \rho - \tau$ , where  $\rho$  and  $\tau$  are reflectivity and transmissivity. A 200 nm thick bottom W layer in the emitter inhibits the light transmission through the emitter, thus absorptivity can be directly obtained from the reflectivity using  $\alpha = 1 - \rho$ .

**Numerical modelling.** Absorptivity/emissivity spectra of the emitter structure for pristine emitter and emitter with voids were calculated using the finite-integration-time-domain method in CST microwave studio. Optical constants of W were taken from Palik data<sup>58</sup>. A unit cell with  $517.5 \times 517.5\ \text{nm}^2$  is constructed to match with the cross-sectional SEM image, and we have implemented 10, 8 and 4 holes with 100 nm diameter in the top three thin W layers, respectively. The unit cell is excited with a plane wave at normal incidence. A fine grid of 40 points per wavelength was chosen to ensure that all results were converging.

**XRD measurements.** XRD measurements were taken using a Bruker D8 Advance diffractometer. Cu K $\alpha$  ( $\lambda = 0.15405\ \text{nm}$ ) radiation with parallel beam geometry was used to characterize the metamaterial structure. The diffraction patterns ( $2\theta$  from  $20^\circ$  to  $80^\circ$ ) were recorded with an increment of  $0.04^\circ$  and a step time of 16 s.

Received: 23 August 2019; Accepted: 12 February 2020;

Published online: 27 February 2020

## References

- Chirumamilla, M. *et al.* Metamaterial emitter for thermophotovoltaics stable up to  $1400^\circ\text{C}$ . *Scientific Reports* **9**, 7241 (2019).
- Arpin, K. A. *et al.* Three-dimensional self-assembled photonic crystals with high temperature stability for thermal emission modification. *Nature Communications* **4**, 2630 (2013).
- Woolf, D. N. *et al.* High-efficiency thermophotovoltaic energy conversion enabled by a metamaterial selective emitter. *Optica* **5**, 213–218 (2018).
- Arpin, K. A., Losego, M. D. & Braun, P. V. Electrodeposited 3D tungsten photonic crystals with enhanced thermal stability. *Chemistry of Materials* **23**, 4783 (2011).
- Rinnerbauer, V. *et al.* High-temperature stability and selective thermal emission of polycrystalline tantalum photonic crystals. *Optics Express* **21**, 11482–11491 (2013).
- Lu, J.-Z. *et al.* Thermal stability investigation of the SS/MO/ $\text{Al}_2\text{O}_3$  spectrally selective solar absorber coatings. *Surface Engineering* **35**, 565–572 (2019).
- Lee, T.-I. *et al.* Pt/Alumina Hyperbolic Metafilms with High-Temperature Stability, Wide Wavelength Tunability, and Omnidirectional Absorption. *Physica Status Solidi (a)* **215**, 1800287 (2018).
- Wells, M. P. *et al.* Temperature stability of thin film refractory plasmonic materials. *Optics Express* **26**, 15726–15744 (2018).
- Green, M. A. & Bremner, S. P. Energy conversion approaches and materials for high-efficiency photovoltaics. *Nature Materials* **16**, 23 (2016).
- Rinnerbauer, V. *et al.* Recent developments in high-temperature photonic crystals for energy conversion. *Energy & Environmental Science* **5**, 8815–8823 (2012).
- Lenert, A. *et al.* A Nanophotonic Solar Thermophotovoltaic Device. *Nature Nanotechnology* **9**, 126 (2014).
- Bierman, D. M. *et al.* Enhanced photovoltaic energy conversion using thermally based spectral shaping. *Nature Energy* **1**, 16068 (2016).
- Fan, S. Thermal Photonics and Energy Applications. *Joule* **1**, 264–273 (2017).
- Fiorino, A. *et al.* Nanogap near-field thermophotovoltaics. *Nature Nanotechnology* **13**, 806–811 (2018).
- Thompson, D. *et al.* Hundred-fold enhancement in far-field radiative heat transfer over the blackbody limit. *Nature* **561**, 216–221 (2018).
- Chubb, D. Fundamentals of Thermophotovoltaic Energy Conversion. 530 (Elsevier Science, 2007).
- Chan, W. R., Waits, C. M., Joannopoulos, J. D. & Celanovic, I. Thermophotovoltaic and thermoelectric portable power generators. *Proceedings of SPIE* **9083**, 90831W (2014).
- Datas, A. & Martí, A. Thermophotovoltaic energy in space applications: Review and future potential. *Solar Energy Materials and Solar Cells* **161**, 285–296 (2017).
- Baranov, D. G. *et al.* Nanophotonic engineering of far-field thermal emitters. *Nature Materials* **18**, 920–930 (2019).
- Utlü, Z., Paralı, U. & Gültekin, Ç. Applicability of Thermophotovoltaic Technologies in the Iron and Steel Sectors. *Energy Technology* **6**, 1039–1051 (2018).
- Bauer, T. Thermophotovoltaics: basic principles and critical aspects of system design. (Springer Science & Business Media, 2011).
- Chou, J. B. *et al.* Enabling Ideal Selective Solar Absorption with 2D Metallic Dielectric Photonic Crystals. *Advanced Materials* **26**, 8041–8045 (2014).
- Zhang, R., Cohen, J., Fan, S. & Braun, P. V. Electrodeposited high strength, thermally stable spectrally selective rhenium nickel inverse opals. *Nanoscale* **9**, 11187–11194 (2017).
- Cao, F. *et al.* A high-performance spectrally-selective solar absorber based on a yttria-stabilized zirconia cermet with high-temperature stability. *Energy & Environmental Science* **8**, 3040–3048 (2015).
- Shimizu, M., Kohiyama, A. & Yugami, H. Evaluation of thermal stability in spectrally selective few-layer metallo-dielectric structures for solar thermophotovoltaics. *Journal of Quantitative Spectroscopy and Radiative Transfer* **212**, 45–49 (2018).
- Kim, J. H., Jung, S. M. & Shin, M. W. High-temperature degradation of one-dimensional metallodielectric (W/SiO<sub>2</sub>) photonic crystal as selective thermal emitter for thermophotovoltaic system. *Optical Materials* **72**, 45–51 (2017).
- Cui, K. *et al.* Tungsten–Carbon Nanotube Composite Photonic Crystals as Thermally Stable Spectral-Selective Absorbers and Emitters for Thermophotovoltaics. *Advanced Energy Materials* **8**, 1801471 (2018).
- Chang, C.-C. *et al.* High-Temperature Refractory Metasurfaces for Solar Thermophotovoltaic Energy Harvesting. *Nano Letters* **18**, 7665–7673 (2018).



29. Omair, Z. *et al.* Ultraefficient thermophotovoltaic power conversion by band-edge spectral filtering. *Proceedings of the National Academy of Sciences* **116**, 15356–15361 (2019).
30. Roberts, A. S. *et al.* Ultra-thin titanium nitride films for refractory spectral selectivity [Invited]. *Optical Materials Express* **8**, 3717–3728 (2018).
31. Chirumamilla, M. *et al.* Multilayer tungsten-alumina-based broadband light absorbers for high-temperature applications. *Optical Materials Express* **6**, 2704–2714 (2016).
32. Ferrari, C., Melino, F., Pinelli, M., Spina, P. R. & Venturini, M. Overview and Status of Thermophotovoltaic Systems. *Energy Procedia* **45**, 160–169 (2014).
33. D. Rahmlo, Jr., T., Lazo-Wasem, J. E., Gratrix, E. J. M. Fourspring, P. & M. DePoy, D. New Performance Levels for TPV Front Surface Filters. *AIP Conference Proceedings* **738**, 180–188 (2004).
34. Sakakibara, R. *et al.* Practical emitters for thermophotovoltaics: a review. *Journal of Photonics for Energy* **9**, 032713 (2019).
35. Kayes, B. M. *et al.* 27.6% Conversion efficiency, a new record for single-junction solar cells under 1 sun illumination. *37th IEEE Photovoltaic Specialists Conference* 000004–000008 (2011).
36. Dyachenko, P. N. *et al.* Controlling thermal emission with refractory epsilon-near-zero metamaterials via topological transitions. *Nature Communications* **7**, 11809 (2016).
37. Park, J. H., Han, S. E., Nagpal, P. & Norris, D. J. Observation of Thermal Beaming from Tungsten and Molybdenum Bull's Eyes. *ACS Photonics* **3**, 494–500 (2016).
38. Chirumamilla, M. *et al.* Large-Area Ultrabroadband Absorber for Solar Thermophotovoltaics Based on 3D Titanium Nitride Nanopillars. *Advanced Optical Materials* **5**, 1700552 (2017).
39. Kim, J. H., Jung, S. M. & Shin, M. W. Thermal degradation of refractory layered metamaterial for thermophotovoltaic emitter under high vacuum condition. *Optics Express* **27**, 3039–3054 (2019).
40. Coppens, Z. J., Kravchenko, I. I. & Valentine, J. G. Lithography-Free Large-Area Metamaterials for Stable Thermophotovoltaic Energy Conversion. *Advanced Optical Materials* **4**, 671–676 (2016).
41. Cho, J.-W. *et al.* Optical Tunneling Mediated Sub-Skin-Depth High Emissivity Tungsten Radiators. *Nano Letters* **19**, 7093–7099 (2019).
42. Leib, E. W. *et al.* Yttria-stabilized zirconia microspheres: novel building blocks for high-temperature photonics. *Journal of Materials Chemistry C* **4**, 62–74 (2016).
43. Dyachenko, P. N. *et al.* Tungsten band edge absorber/emitter based on a monolayer of ceramic microspheres. *Optics Express* **23**, A1236–A1244 (2015).
44. Wang, J., Li, H. P. & Stevens, R. Hafnia and hafnia-toughened ceramics. *Journal of Materials Science* **27**, 5397–5430 (1992).
45. Brace, D. B. *The Laws of Radiation and Absorption: Memoirs by Pre' vost, Stewart, Kirchhoff, and Kirchhoff and Bunsen.* (American Book Company, 1901).
46. Siegel, R. & Howell, J. *Thermal Radiation Heat Transfer.* (Hemisphere Publishing Corporation, New York, 1981).
47. Lu, Q. *et al.* InAs thermophotovoltaic cells with high quantum efficiency for waste heat recovery applications below 1000 °C. *Solar Energy Materials and Solar Cells* **179**, 334–338 (2018).
48. Yakubovskiy, D. I., Arsenin, A. V., Stebunov, Y. V., Fedyanin, D. Y. & Volkov, V. S. Optical constants and structural properties of thin gold films. *Optics Express* **25**, 25574–25587 (2017).
49. Reddy, H., Guler, U., Kildishev, A. V., Boltasseva, A. & Shalae, V. M. Temperature-dependent optical properties of gold thin films. *Optical Materials Express* **6**, 2776–2802 (2016).
50. Langford, J. I. & Wilson, A. J. C. Scherrer after sixty years: A survey and some new results in the determination of crystallite size. *Journal of Applied Crystallography* **11**, 102–113 (1978).
51. Jeffery, G. A. Elements of x-ray diffraction (Cullity, B. D.). *Journal of Chemical Education* **34**, A178 (1957).
52. Rekus, J. F. *Complete Confined Spaces Handbook.* (CRC Press, 1994).
53. Kharton, V. V., Yaremchenko, A. A., Naumovich, E. N. & Marques, F. M. B. Research on the electrochemistry of oxygen ion conductors in the former Soviet Union. *Journal of Solid State Electrochemistry* **4**, 243–266 (2000).
54. Foster, A. S., Lopez Gejo, F., Shluger, A. L. & Nieminen, R. M. Vacancy and interstitial defects in hafnia. *Physical Review B* **65**, 174117 (2002).
55. Kellett, E. A. & Rogers, S. E. The Structure of Oxide Layers on Tungsten. *Journal of Electrochemical Society* **110**, 502–504 (1963).
56. Cifuentes, S. C., Monge, M. A. & Pérez, P. On the oxidation mechanism of pure tungsten in the temperature range 600–800 °C. *Corrosion Science* **57**, 114–121 (2012).
57. Tumkur, T., Barnakov, Y., Kee, S. T., Noginov, M. A. & Liberman, V. Permittivity evaluation of multilayered hyperbolic metamaterials: Ellipsometry vs. reflectometry. *Journal of Applied Physics* **117**, 103104 (2015).
58. Palik, E. D. *Handbook of Optical Constants of Solids.* (1985).

## Acknowledgements

The authors gratefully acknowledge financial support from the Deutsche Forschungsgemeinschaft (DFG, German Research Foundation) – Projektnummer 192346071 – SFB 986, and by Open Access Fund of Hamburg University of Technology (TUHH). We acknowledge the sponsorship from Dassault Systems by providing the CST Studio Suite simulation software.

## Author contributions

M.C., A.Y.P., and M.E. designed the experiments. G.V. and M.S. fabricated the thin-film metamaterial structures, performed XRD measurements and analyzed the diffraction patterns considering phase formation and structural alterations. M.C. investigated the optical properties of the emitter. S.R. and M.R. performed cross-sectional SEM imaging. M.C., A.Y.P. and M.E. performed the analysis, and M.E. supervised the project. M.C. wrote the manuscript draft, all authors discussed the manuscript and provided adaptations for its finalization.

## Competing interests

The authors declare no competing interests.

## Additional information

**Correspondence** and requests for materials should be addressed to M.C.

**Reprints and permissions information** is available at [www.nature.com/reprints](http://www.nature.com/reprints).

**Publisher's note** Springer Nature remains neutral with regard to jurisdictional claims in published maps and institutional affiliations.



**Open Access** This article is licensed under a Creative Commons Attribution 4.0 International License, which permits use, sharing, adaptation, distribution and reproduction in any medium or format, as long as you give appropriate credit to the original author(s) and the source, provide a link to the Creative Commons license, and indicate if changes were made. The images or other third party material in this article are included in the article's Creative Commons license, unless indicated otherwise in a credit line to the material. If material is not included in the article's Creative Commons license and your intended use is not permitted by statutory regulation or exceeds the permitted use, you will need to obtain permission directly from the copyright holder. To view a copy of this license, visit <http://creativecommons.org/licenses/by/4.0/>.

© The Author(s) 2020